



Optical MIDO – Multiple Inputs - Digital Output – device

A. M. Alaíz-Gudín* , A. P. González-Marcos 

Photonic Technology and Bioengineering Department, Universidad Politécnica de Madrid (UPM), Madrid, 28040 Spain

Article info

Article history:

Received 12 Sep. 2021

Received in revised form 29 Sep. 2021

Accepted 29 Sep. 2021

Available online 2 Nov. 2021

Keywords:

distributed feedback laser, multi quantum well, optical bistability, semiconductor laser.

Abstract

Advances in photonic technologies, with new processes and scopes of photonic integrated circuits, have generated a lot of interest as the field allows to obtain sensors with reduced size and cost and build systems with high interconnectivity and information density. In this work, answering the needs of photonic sensors that must be portable, more energy-efficient, and more accurate than their electrical counterparts, also with a view to the emerging field of neuromorphic photonics, a versatile device is presented. The proposed device makes use of the well-known advantages provided by optical bistability. By combining two distributed feedback-multi quantum well semiconductor laser structures, this new optical multiple inputs - digital output device offers various essential purposes (such as logic gates, wavelength detector and monitoring) with no need for specific manufacturing for each of them. Through a commercial computer-aided design tool, VPIphotonics™, the necessary characterization of proposed device is also described.

1. Introduction

In this work, a photonic device, a Multiple Inputs - Digital Output device (MIDO), is described and characterized. It is composed of two semiconductor laser diodes (LDs) that show the optical bistability effect. Studies about optical bistability in LDs started in the 1960s of the 20th century [1]. However, the most relevant research articles, mainly passive bistability, e.g., see the survey [2], were written afterward during the 1980s; some of the early papers on optical semiconductor oscillators and amplifiers were also developed in the course of that time [2–5]. During the following decade, optical bistability was a recurrent research topic because of its potential applications in several fields, for example, optical computing and optical communications, and because of the inherent advantages of laser amplifiers, such as their gain, fast response, low optical power necessary to obtain bistability [6, 7].

Regarding Boolean algebra, in particular logic gates, in 1985 an ideal digital optical device based on the preservation of the optical bistability and non-linear gain in a semiconductor laser amplifier (SLA) was proposed [8].

It included non-inverting logic (such as AND and OR) and inverting logic (NAND and NOR Boolean functions). Experimental demonstration of the logic operation with an SLA was reported for the first time in 1986 [9]. That work presented an all-optical AND logic gate. In 1987, Inoue [10] reported inverting logic using an SLA under the injection of two input beams at different wavelengths.

Development of basic units capable of providing several logic functions in a flexible way is an important objective to obtain versatility. The design of the flexible logic device based on the hysteresis provided by the optical bistability, an antecedent of the MIDO device, has made it possible to propose different applications, such as half-adders and full adders in an arithmetic unit [11], optical digital chaos generator [12], coder-decoder in information systems [13], add-drop multiplexer for wavelength division multiplexing (WDM) [14]. Finally, in connection with the emerging field of neuromorphic photonic technology [15], the application of this device as a neuron model in a mammalian retina model was proposed in Ref. 16. It is worth noting that the previous work was based on theoretical and functional behaviour demonstration using Simulink™ and built with some optoelectronic devices. On the other hand, this work uses new photonic technologies and simulation tools (in particular, VPIphotonics™).

*Corresponding author at: am.alaiz@alumnos.upm.es

The paper is structured as follows. Section 2 reviews optical bistability, especially in distributed feedback (DFB) structures, use of the MIDO device as a reconfigurable logic device, and tools used. Section 3 contains a description of the MIDO device structure, study of the characterization of each bistable device (BD) forming the MIDO device, and MIDO device itself. It also includes a description of the device operation and its versatility. Finally, section 4 presents the application of the MIDO device in different fields: logic gates, wavelength detector, and monitoring. The paper ends with some conclusions.

2. Preliminaries

2.1. Optical bistability in laser diodes

Although recent studies have obtained a resonator-free bistability [17], generally to obtain bistability, two phenomena are necessary: nonlinearity and optical feedback. Bistability is two different output states for the same input over the range of input values [2]. The two kinds of optical bistability depending on the nonlinearity are: absorptive and dispersive.

In the first case, the cause of bistability is the dependence of the absorption coefficient on input light intensity in a laser with a saturable absorber. This bistability was observed for the first time in a Fabry-Pérot semiconductor laser with external optical injection in the 1960s [1], and it was experimentally demonstrated in a two-section distributed feedback (DFB) laser [18]. This bistability has been proved in both output power/current characteristics [3] and output/input power characteristics [19] (more information about this type of bistability can be found in, e.g., Ref. 20).

On the other hand, dispersive bistability is caused by a dependence on intensity of the refractive index which shifts the cavity frequency towards resonance with the input field. It was first studied theoretically in SLAs at a wavelength of 840 nm [21] and 820 nm [22] in 1983. Later, it was also demonstrated in a Fabry-Pérot SLA at 1.3 μm [9] and in an InGaAsP Fabry-Pérot laser amplifier at 1.5 μm [23,24]. Previous to the present study, structures with different semiconductor lasers similar to the MIDO device structure have been studied: with vertical-cavity semiconductor optical amplifier (VCSOA) and distributed feedback semiconductor optical amplifier (DFBSOA) [25], with bulk and with quantum well (QW) [26]. The main feature of a distributed feedback (DFB) semiconductor laser is a high spectral purity. They have been intensely studied theoretically and experimentally in the last three decades [27,28].

In this work, the laser structure is DFB, where there is a surface corrugation grating embedded very close to the active region, usually formed by a multi quantum well (MQW). DFB lasers emit an optical signal with a very narrow linewidth and a wavelength with low sensitivity to shifts in drive current [29–32]. Due to this, the DFB laser is the best suited optical source in optical communications, microwave photonics, and photonic sensing [33–36]. For these reasons, the work described in this paper focuses on analysing the MIDO device consisting of two DFB-MQW lasers.

2.2. Optical bistability in a DFB-MQW laser

Although there are different types of bistability cycles [25], this work focuses only on two of them, clockwise (Z-shape) and anticlockwise (S-shape), see Fig. 1.

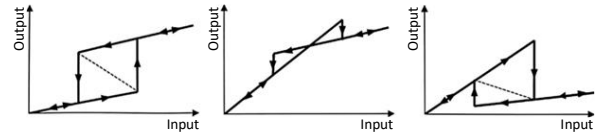


Fig. 1. Bistable cycle shapes: anticlockwise (S-shape), butterfly (X-shape), and clockwise (Z-shape) [25].

Depending on whether the BD signal is transmitted or reflected, and its bias current, it will show two different bistability cycles: clockwise for the transmitted signal (BD2) and anticlockwise for the reflected one (BD1), as shown in Fig. 1.

As described above, different BD structures were studied to take advantage of the optical bistability, such as VCSOA and DFBSOA [25], bulk, and QW [26]. In this case, MQW-DFB forms a BD structure. For an exhaustive study of the MQW-DFB lasers, the readers can refer to Refs. 27 and 28 where they have been widely studied. This section, which does not intend to be an exhaustive study of these well-known lasers, explains the bases and parameters used in the MIDO device.

First, it should be mentioned that the grating phase shift used is 90°, illustrated in Fig. 2. The reason is that it offers a single resonance frequency instead of two, which would split the power offered by the laser in our applications, as shown in Fig. 3.

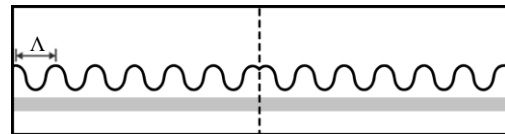


Fig. 2. Schematic diagram showing the grating phase shift of the DFB laser section. Modified from Ref. 28.

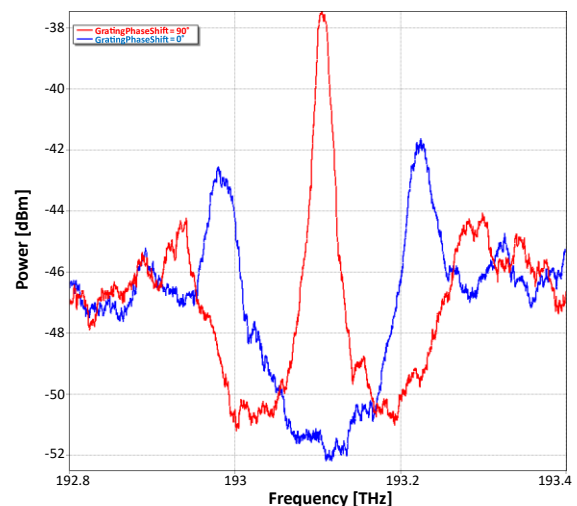


Fig. 3. Variation of the grating phase shift in BD2.

As explained in the previous section, the two MQW–DFB lasers used have different configurations. The first parameter in which they differ is the Bragg period (A). This parameter is directly related to the resonance frequency, known as Bragg frequency (ν_B), according to $\lambda_B = 2n_e A$, where λ_B is the Bragg wavelength ($\lambda_B = c/\nu_B$), and n_e is the effective refractive index. Therefore, through the Bragg period, the laser can be placed at the optimum working point for the functionality of the MIDO device. Moreover, it is also essential to consider the effect of the input power in the laser: $n_e = n_0 + n_2 P_{in}$, where n_0 is the refractive index for low P_{in} (input power) values and n_2 is the nonlinear refractive index. When the input power increases, n_e also increases, so the Bragg frequency decreases, see Fig. 4(a)–(c). However, on the other hand when it decreases, the Bragg frequency increases, see Fig. 4(d). Fig 18 in subsection 3.4 shows the actual power ratio.

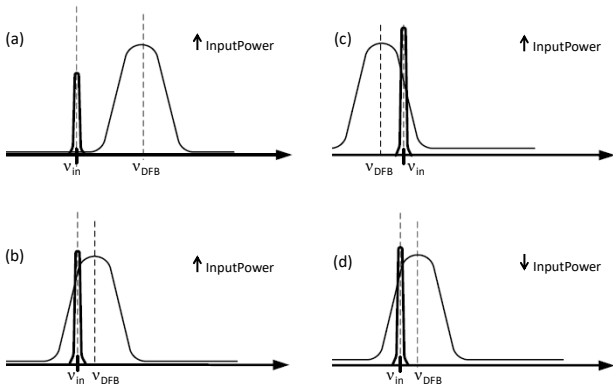


Fig. 4. Input power effect in Bragg frequency. Increasing input power, so Bragg frequency decreases (a)–(c), and decreasing input power, so Bragg frequency increases (d).

2.3. Reconfigurable logic device

One of the essential applications of the MIDO device is its use as a reconfigurable logic gate in the optical domain directly. Its flexible and dynamical behaviour has already been well described with different BD structures in Refs. 12 and 26. Briefly, in this work, this device consists of the three optical signals shown in Fig. 5: two optical digital input signals, I_1 and I_2 , with the data to process, and one optical control signal, g . The output optical signal, O_{MIDO} , is the logic function determined by the level of the control signal.

The internal structure of the reconfigurable logic device, shown in Fig. 6, corresponds to the internal configuration of the MIDO device proposed and described in this work. Each BD has a different purpose, with a different transfer function, depending on the control signal and its bias current (or another parameter). For a detailed explanation, Ref. 12 can be referred, as well.

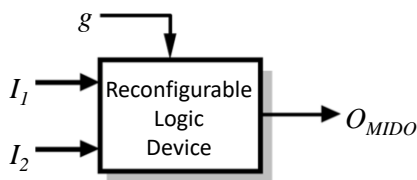


Fig.5. Functional structure of the reconfigurable logic device.

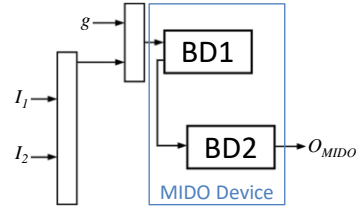


Fig. 6. Internal structure of the reconfigurable logic device with two bistable devices.

For low values of input signals ($d_{MIDO1}/2$), only the ideal BD2 effect appears, as illustrated in Fig. 7. The logic function is determined by the control signal g , with only three levels (g_0, g_1 , and g_2). Figure 8 shows the ideal transfer function of the MIDO with both BDs effects. In this case, the decision levels in the figures are equidistant, with $d_{MIDO2}=2d_{MIDO1}$, $d_{MIDO3}=3d_{MIDO1}$, and $d_{MIDO4}=4d_{MIDO1}$ and the logic function is determined by g , which has five levels (g_0, g_3, g_4, g_5 , and g_6). The effect of input signals with double amplitude is shown in Fig. 9. In this case, the control signal g has five levels (g_0, g_7, g_8, g_9 , and g_{10}), four different from the configuration shown in Fig. 8.

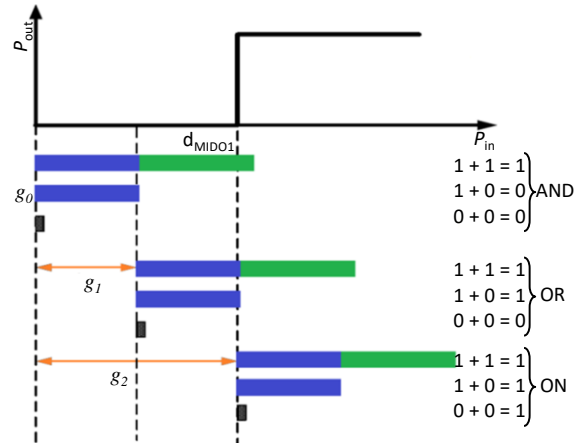


Fig. 7. MIDO ideal transfer function for input signals with an amplitude of $d_{MIDO1}/2$.

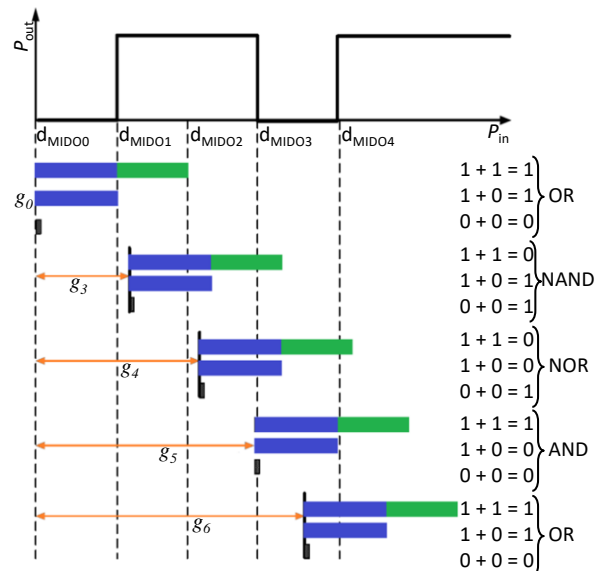


Fig. 8. MIDO ideal transfer function.

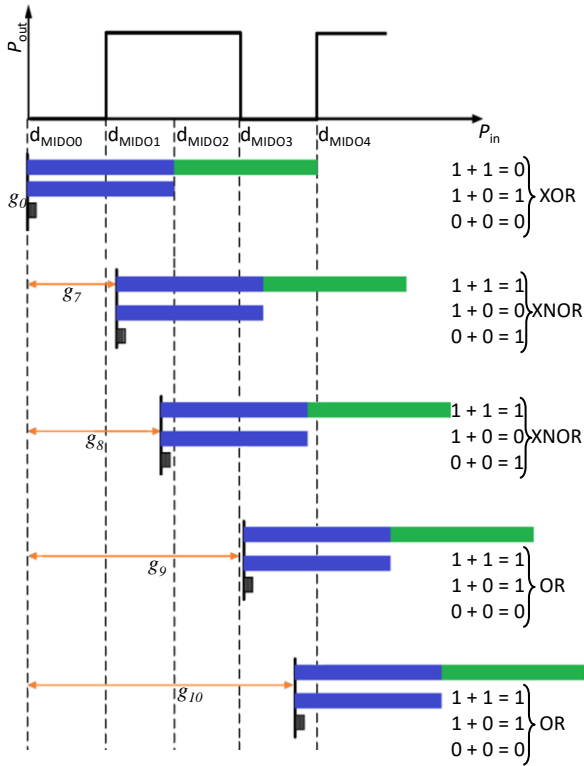


Fig. 9. MIDO ideal transfer function for input signals with an amplitude of $2d_{MIDO1}$.

Due to all the applications of the reconfigurable logic device, there have been several studies, developments, and improvements of the internal structure of this device with different BD structures, as previously shown, like VC SOA and DFBSOA [25], bulk, and QW [26]. The logic functions AND, using input signals with a single amplitude for data signals, and XOR, using input signals with a double amplitude for data signals are described in section 4.1.

2.4. Simulation tools

The evolution of simulation models of the photonic devices and systems behaviour is highly developed, although many aspects are not covered as thoroughly as in the electrical domain. They already offer the advantages of computer-aided design (CAD) tools that allow checking the behaviour of the system design before carrying out the expensive experimental tests that require both equipment and time to search for operating conditions.

The CAD tool VPIphotonics™, used in this work, allows the design, implementation, and simulation of various fibre-optic networks and optical components, using a predefined library and updated to new technologies. One of its necessary advantages to simulate these effects is having "memory": obtaining simulation data from a particular instant depends on previous moments. This advantage is essential since the BD current level depends on the level that the device had previously.

However, the issue of temperature, and mechanical strength, cannot be considered in the simulations of the used software, as in the usual CAD tools, since this would require parallel processing. In practice, it is necessary to stabilize the temperature or verify that the device is not affected by a temperature variation (as shown in other devices [37–39]).

Moreover, variations in the medium parameters with the polarization of the beam have not been considered. The input signals have 0° azimuth and ellipticity in polarization. In this way, only the X polarization influences the measurements obtained.

3. MIDO device

3.1. MIDO device structure

The MIDO device was first described in the International OSA Network of Students 58 (2015). Its transfer function $P_{out}(P_{in})$ is similar to the one presented by a self-electrooptic effect device (SEED), devices within its bistable behaviour [40]. In this work, bias current parameter of the BDs, initial phase detuning, and Bragg grid characteristics are initially characterized and not modified later. A diagram of the MIDO device, where the BDs are DFB–MQW lasers is shown in Fig. 10. Previous studies have been carried out using a material with similar MQW parameters to those used in this paper, with linear and nonlinear gain [41], as well as the behaviour of a bulk cavity with InGaAsP material [42]. In particular, the reflected output signal of the first one is injected into the second one. Due to the importance of good characteristics of the MIDO device, the behaviour of both BDs is studied.

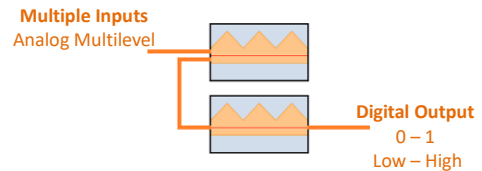


Fig. 10. Scheme of the MIDO device.

3.2. Characteristics of bistable device 1 – reflection of the LD device

The reflected signal of the BD1 is the input signal of the BD2. Table 6, in Appendix , contains the parameters of both BDs used to obtain the MIDO device. Most of the parameters are set to the default value offered by the simulation program [43], and only those related to its manufacture (such as width, length) were tuned. In addition, Appendix contains the meaning of each parameter used in the simulations.

In order to obtain a power drop in the output signal, enough to allow the BD2 to generate two bistability cycles, the bias current of the BD1 is below 40% of its threshold current. With a greater bias current, the behaviour would not show any drop necessary to obtain a characteristic curve of the MIDO device, as it is shown in Fig. 11.

Before showing the variation effect of the BD1 bias current (I_p), in Fig. 12, the threshold current (I_{th}) for the parameters of Table 6 (BD1) is shown.

In Fig. 13 and Table 1, the polarization current variation effect in the BD1 is shown. It can be seen, that the bias current must drop suddenly enough to produce two bistability cycles due to the BD2 effect. Although most BD parameters can be varied to see its effect, this paper focuses on the variation of the polarization current. Thus, the versatility of the BD can be appreciated by just varying one parameter.

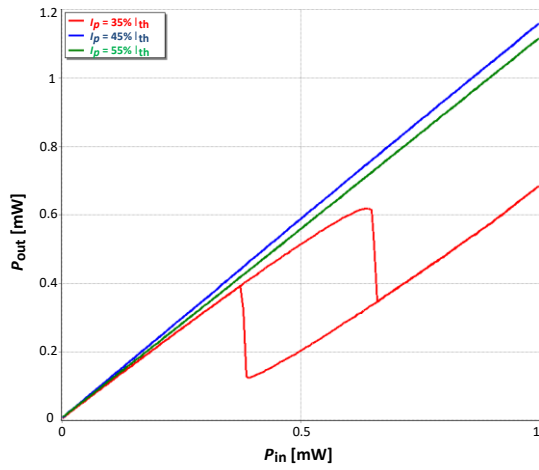


Fig. 11. BD1 characteristic curves depending on bias current (I_p).

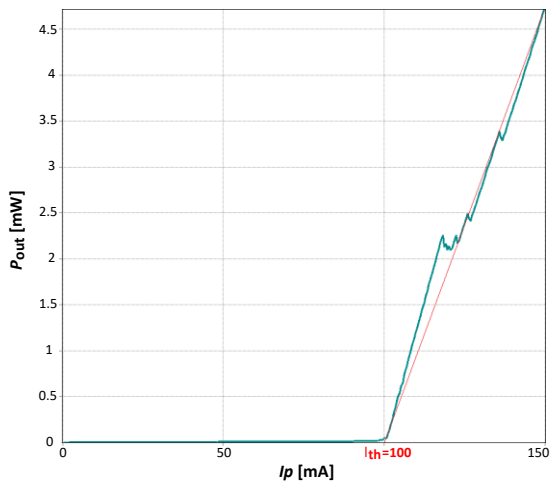


Fig. 12. BD1 threshold current (I_{th}).

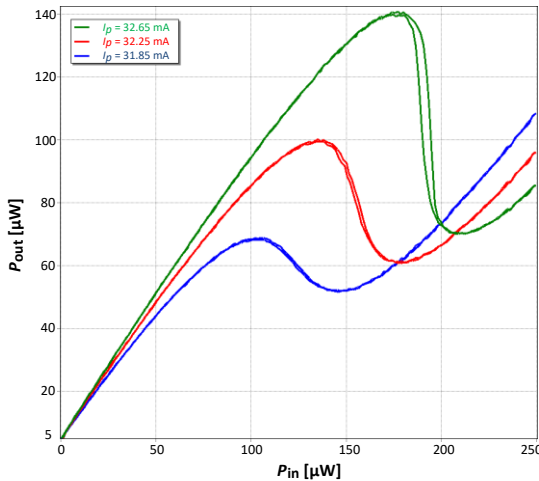


Fig. 13. Variation of polarization current in BD1.

Table 1.
BD1 hysteresis curve.

I_p	ΔP_{in} (width)	ΔP_{out} (contrast)
31.85 mA	–	16.54 μ W
32.25 mA	–	39.51 μ W
32.65 mA	4.8 μ W	

3.3. Characteristics of bistable device 2 – transmission of the LD device

Two cycles of bistability are obtained using this BD, by receiving as an input the signal reflected from BD1. Generation of a bistability cycle was achieved before the power output curve BD1 was lowered and another cycle after this lowering. The working point is obtained with a bias current of approximately 45% of the threshold current. In Fig. 14, the threshold current for the parameters of Table 6 (BD2) is shown. Regarding the BD2, the polarization current variation effect is shown in Fig. 15 and Table 2. In this case, the need for the bias current is not as low as for the BD1.

Again, the polarization current variation is studied in this paper while the remaining parameters are fixed to the values shown before, so the BD versatility can be appreciated

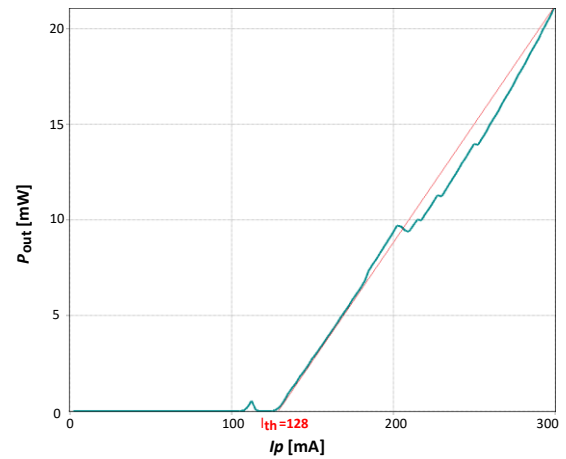


Fig. 14. BD2 threshold current (I_{th}).

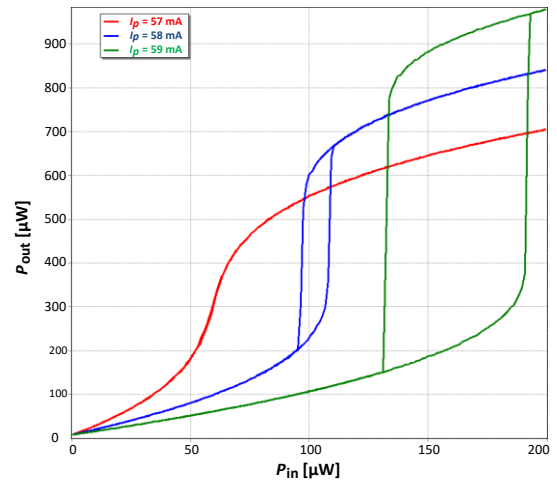


Fig. 15. Variation of a polarization current in BD2.

Table 2.
BD2 hysteresis curve.

I_p	ΔP_{in} (width)	ΔP_{out} (contrast)
57 mA	–	267 μ W
58 mA	10.8 μ W	473.19 μ W
59 mA	58.8 μ W	

3.4. MIDO device

Combining the effects of two BDs described above, Fig. 16 shows the MIDO device characteristics curve. The first and third cycles of hysteresis, caused by the effect of BD2, are anti-clockwise. The second, caused by BD1, is clockwise. These hysteresis cycles, and, therefore, MIDO device behaviour, can be freely modified with the modification of any parameter, as it has been seen in the case of the bias current (I_p) illustrated in Fig. 17. That gives the MIDO device a versatility that allows it to be used in a wide variety of applications.

These two figures show that the ideal performance seen in Fig. 8 and Fig. 9 is not achieved in practice. However, that does not prevent the device from behaving correctly in the applications shown in the subsequent section.

As said before, Fig. 17 shows the variation in the behaviour of the MIDO device depending on the bias currents. In the first case ($I_{p1} = 32.47$ mA, $I_{p2} = 60$ mA), the BD2 effect occurs after the drop produced by BD1, so it shows only one bistable cycle. In contrast with the second case ($I_{p1} = 32.47$ mA, $I_{p2} = 56$ mA), the BD1 effect occurs before the BD2 effect; however, this first drop is not abrupt enough to produce another bistable cycle. In the third case ($I_{p1} = 32.67$ mA, $I_{p2} = 58$ mA), we can appreciate how the

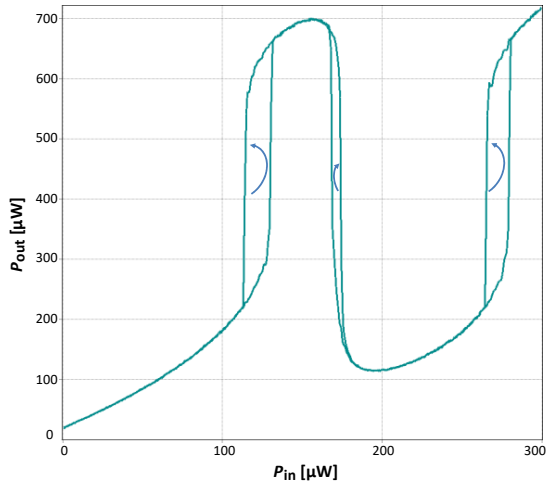


Fig. 16. DFB-MQW MIDO device.

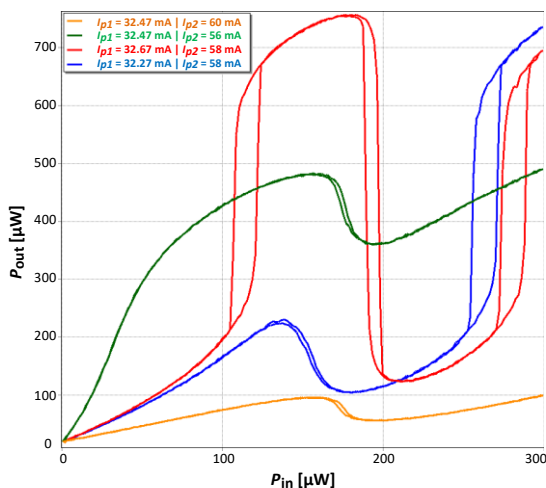


Fig. 17. MIDO device characteristic curves depending on the bias currents (I_p).

second bistable cycle is shifted to the right due to a bias current bigger than the one used in Fig. 16. The last case ($I_{p1} = 32.27$ mA, $I_{p2} = 58$ mA) shows similar behaviour to the first case because the lower value of the I_{p1} makes BD1 drop before the BD2 effect.

In what follows, the optical spectrum of the MIDO device output signal is studied. Depending on the input state, and thus, the output, the injected signal frequency coincides with the resonance frequency of the laser. Thanks to the Bragg frequency variation, explained at the beginning of the paper, the effect of coinciding or not both frequencies produces the MIDO device characteristics curve.

Figure 18 shows such an optical spectrum after a rectangular filter of 3 GHz. The spectrum is shown in four points: without any input signal (P_{in_0}), in the first high output section (P_{in_A}), in the low output (P_{in_B}), and in the last high output section (P_{in_C}).

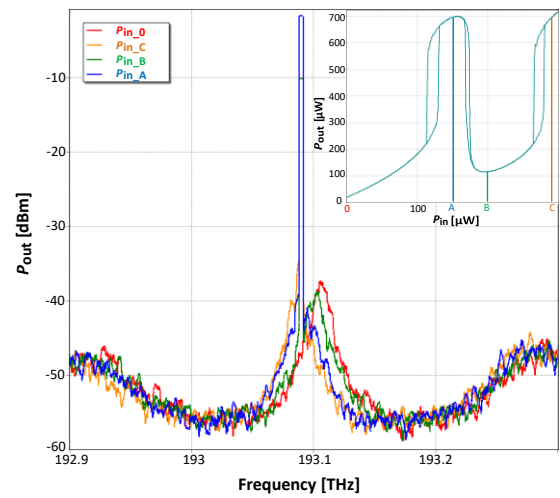


Fig. 18. DFB-MQW MIDO device optical spectrum.

4. MIDO device applications

Some of this device applications have been studied in previous years for similar structures with different BDs such as switching and optical computing [25], neuronal modal [15], and, more recently, the importance of photonic technology in the defence field [44]. Due to the MIDO device versatility, its use is not limited to these applications and could be extended to other applications.

4.1. Logic gates

Thanks to the configuration of the MIDO device, it can be used as a logic gate; with a control signal, the working point is placed according to the selected logic gate function. The two input signal levels will be doubled in the second case, as explained before.

Although any type of logic gates could be studied, only the following two are addressed: AND and XOR gates. In Fig. 19, the chosen level of the control signal and the levels of the input signals can be seen.

Simulations at the speed of 125 Mbps have been carried out to verify the logic gate functions, whose satisfactory results are shown in Fig. 20 (AND gate) and

Fig. 21 (XOR gate) with main parameters summarized in Table 3. InputSignal1 has 011 codification while InputSignal2 has 001.

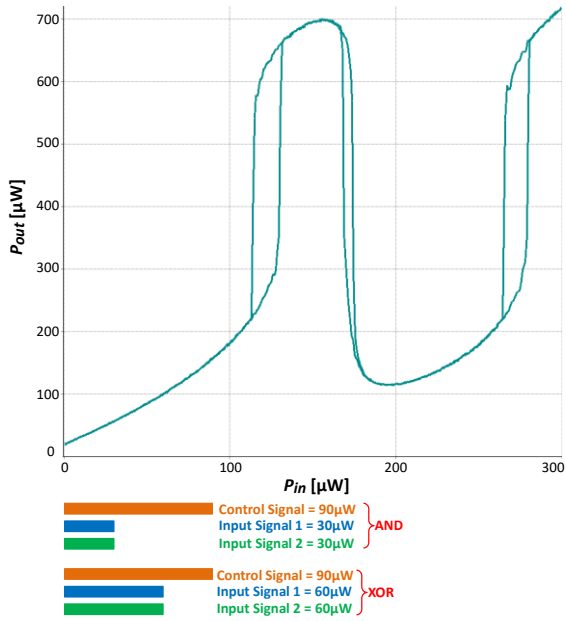


Fig. 19. Top: MIDO device characteristics curve. Bottom: control and input signal amplitudes for AND and XOR logic gate configuration.

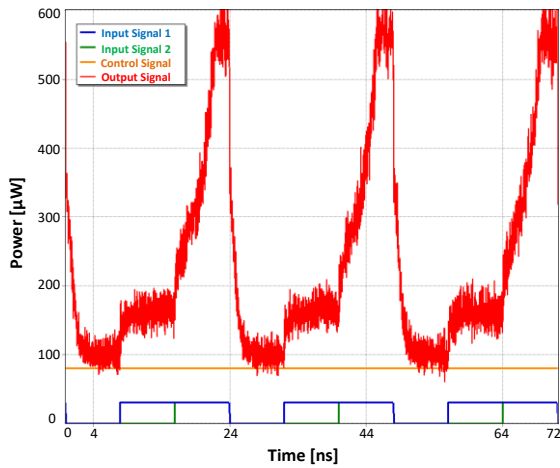


Fig. 20. AND logic gate at 125 Mbps.

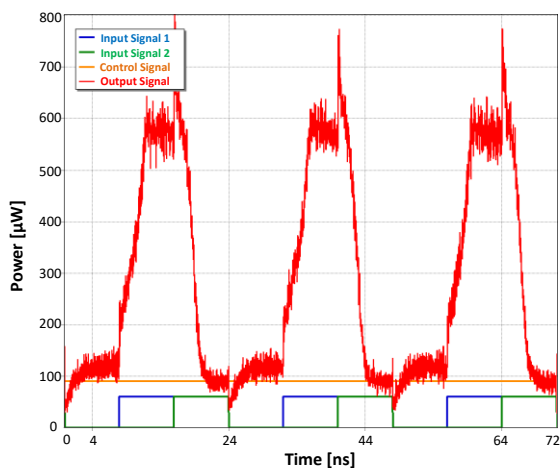


Fig. 21. XOR logic gate at 125 Mbps.

Table 3. MIDO device main parameters acting as logic gates.

Parameter	Value
P_{in}	30 µW
P_{out} high-level	>500 µW
P_{out} low-level	<200 µW

4.2. Wavelength detector

This section presents the MIDO device acting as a sensor, in particular as a wavelength detector. As shown in Fig. 22, the operation is the following: the sensor will be formed by the MIDO device where a signal is injected (detector signal – λ_D). A signal (sensed signal – λ_S) with much lower power than the detector signal is injected at the sensor input. When the wavelength of both signals is the same ($\lambda_S = \lambda_D$), the output signal will be at a high level, and it will return to the low level when they are not the same ($\lambda_S \neq \lambda_D$).

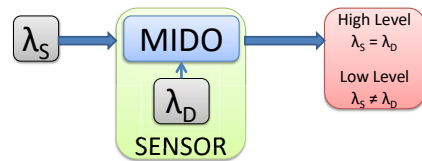


Fig. 22. Scheme of the wavelength detector.

The signal at the wavelength detector input is optical, as it is its response, and it can come from the wavelength detector reference source or an external source. The signal is introduced and extracted from the medium under study through a fibre. This fibre can act as a sensor or capture the reflection and transmission of the signal that directly affects the said medium, as shown in Fig. 23. When calibrating the wavelength detector, the output level is associated with the presence or absence of a certain wavelength, and thus, due to its sensitivity, it can immediately detect that the medium under test induces wavelength variations.

The operation of this detector is as follows: by adjusting and correctly calibrating it, it will be able to be

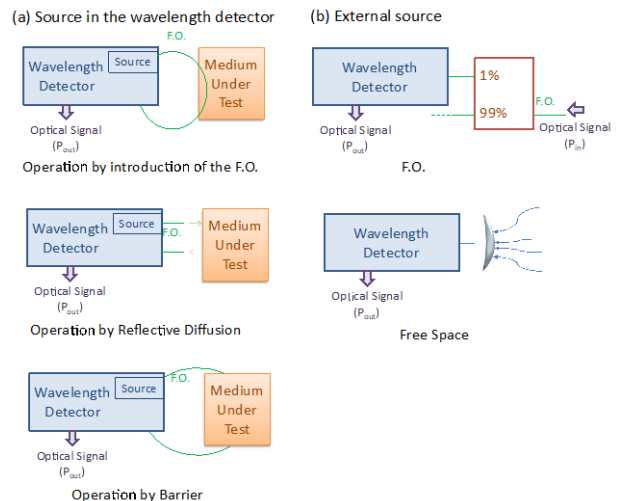


Fig. 23. Types of input signal of the wavelength detector: source in the wavelength detector (a), external source (b).

centred on a certain wavelength. Showing small variations in this wavelength can immediately detect any change in the medium where another sensor works, such as fibre, see the configuration of Fig. 23(a). It is also valid to obtain the signal from another source external to the device, directly from the environment or a communication line or a sensor network, and check the presence of a certain wavelength, which would correspond to the calibration of the wavelength detector, as shown in Fig. 23(b).

With the ability to scan, within the wavelength range, in the wavelength detector concept with a single wavelength, a tunable detector is obtained.

However, in some scenarios where detector tuning does not matter, the detector acts as an alarm system. In these cases, the wavelength is fixed for a certain value, and any variation would be shown. These variations occur due to common parameters changes, by temperature or pressure, or even by changes in the environment, so that certain elements that were not previously present in the environment can be seen as soon as they appear, for example, elements to be identified as some harmful gases.

As an alarm system, it can work in two configurations: either in a hostile environment or in an environment where the correct operating margin is very small. In the first case, as long as the desired wavelength is detected, it will be safe, see Fig. 24(a). In the other case, the detection of a certain wavelength warns against dangerous situation. Thus, in this case, the detector would be used as an analyser to indicate the presence of dangerous elements, useful for detecting toxic or harmful materials, see Fig. 24(b).

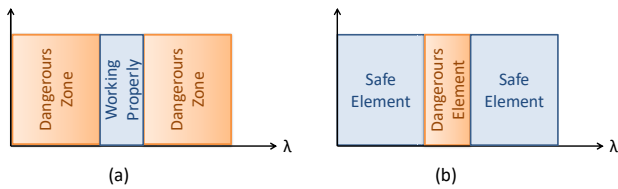


Fig. 24. Types of wavelength detector operating as an alarm system.

The power of the sensed signal is of 100 μW, and the detector is tunable in more than 8 GHz, as shown in Fig. 25. The difference between the low-level and the high-level power will always be greater than 500 μW (see other data in Table 4). The accuracy of the detector is less than 110 MHz.

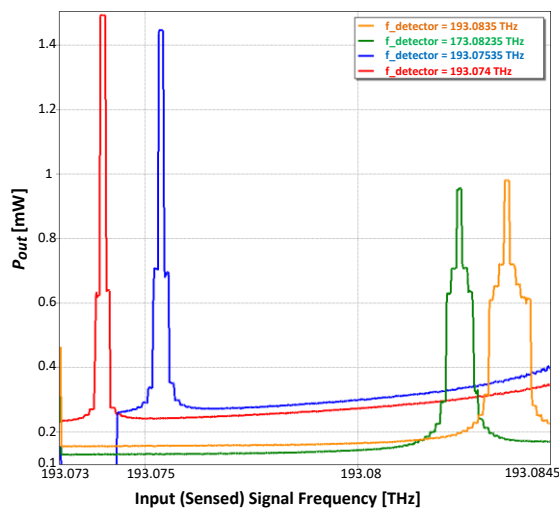


Fig. 25. Wavelength detector.

Table 4. MIDO device main parameters acting as a wavelength detector.

Parameter	Value
Sensed signal power	100 μW
MIDO device P_{out} high-level	>900 μW
Tunable bandwidth	>8 GHz
Detector accuracy	<110 MHz

4.3. Wavelength monitoring

This section presents the use of the MIDO device as a wavelength monitor, as it was studied in Ref. 25 with a similar structure. In this case, unlike the previous section, a signal would be directly analysed to study its wavelength shift. Different levels of the permitted band extremes allow knowing if the variation is due to an increase or a decrease in its wavelength. Therefore, the wavelength of the signal under test can be monitored.

If the frequency of the input signal injected into the MIDO device is inside the permitted frequency band, the output signal will be at a low-level (less than 300 μW), so-called '0'. If the signal frequency is reduced, it will remain at a low-level until it abruptly rises to a high-level (higher than 800 μW), so-called '2'. This abrupt rise indicates that the frequency has decreased. On the other hand, if the signal frequency increases, it will remain at a low-level until it abruptly rises to a different high-level, (equal to 520 μW), so-called '1'. This abrupt rise reflects that the frequency has increased.

Figure 26 shows this MIDO device application, and its effect is shown in Fig. 27 with summarized main parameters in Table 5.

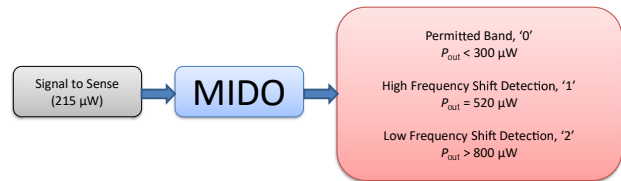


Fig. 26. Scheme of the MIDO device acting as a wavelength monitoring.

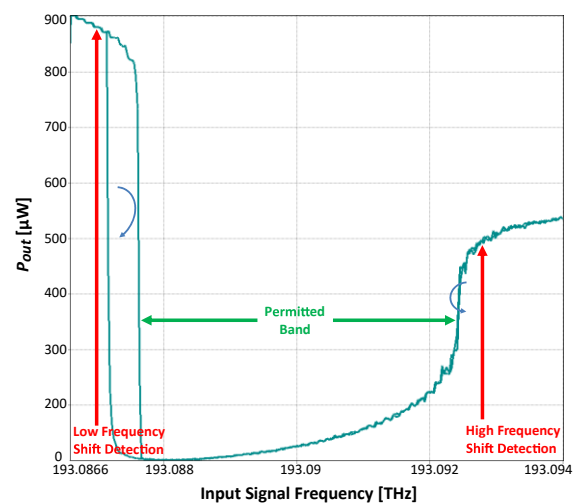


Fig. 27. Wavelength monitoring.

Table 5.
MIDO device main parameters acting as a wavelength monitoring.

Parameter	Value
Input signal power	225 μ W
Low frequency shift detection P_{out}	>800 μ W
Permitted band P_{out}	<300 μ W
Permitted bandwidth	>40 GHz
Protection bandwidth	<700 MHz

Due to the hysteresis cycles, there will not be any repetitive change between the low-output level, '0', and the high-levels, '1' and '2', which benefits the stability of the monitor (protection bandwidth).

5. Conclusions

In this study, the MIDO device has been characterized showing its versatility by varying only one of its parameters, the bias current. By varying the rest of its parameters, the MIDO device could have many new possible applications in different fields, such as optical computing or photonic sensors; this is a line of the future work that should be explored.

Formed by two bistable devices (BDs), which are as well-known and studied as the MQW–DFB lasers, it is based on a mature technology that already allows fabricating prototypes with no need for more development. Three important applications of the MIDO device have been described, showing the impact this device may have in practice: configurable logic gate, wavelength detector, and wavelength monitor.

Acknowledgements

The authors would like to thank the Life Supporting Technologies Group (LST-UPM) for the VPIphotonics™ license.

References

- [1] Lasher, G. J. Analysis of a proposed bistable injection laser. *Solid State Electron.* **7**, 707–716 (1964). [https://doi.org/10.1016/0038-1101\(64\)90027-9](https://doi.org/10.1016/0038-1101(64)90027-9)
- [2] Gibbs, H. M. *Optical bistability: Controlling light with light*. Orlando, FL: Academic (Academic Press, INC., 1985). <https://doi.org/10.1063/1.2820150>
- [3] Kawaguchi, H. & Iwane, G. Bistable operation in semiconductor lasers with inhomogeneous excitation. *Electron. Lett.* **17**, 167–168 (1981). <https://doi.org/10.1049/el:19810117>
- [4] Lattes, A., Haus, H. A., Leonberger, F. J. & Ippen, E. P. An ultrafast all-optical gate. *IEEE J. Quantum Electron.* **19**, 1718–1723 (1983). <https://doi.org/10.1109/jqe.1983.1071766>
- [5] Wang, S. W., Wang, C. & Ling, S. Stability analysis of semiconductor bistable lasers. *IEEE J. Quantum Electron.* **23**, 1033–1038 (1987). <https://doi.org/10.1109/jqe.1987.1073447>
- [6] Hui, R. Static and dynamical properties of dispersive optical bistability in semiconductor lasers. *J. Light. Technol.* **13**, 42–48 (1995). <https://doi.org/10.1109/50.350648>
- [7] Li, L. Optical frequency bistability and power bistability in semiconductor lasers. *IEEE J. of Quantum Electron.* **31**, 233–239 (1995). <https://doi.org/10.1109/3.348050>
- [8] Midwinter, J. E. 'Light' electronics, myth or reality? *IEE Proc., J. Optoelectron.* **132**, 371–383 (1985). <https://doi.org/10.1049/ip-j.1985.0070>
- [9] Sharfin, W. F. & Dagenais, M. Room-temperature optical bistability in InGaAsP/InP amplifiers and implications for passive devices. *Appl. Phys. Lett.* **46**, 819–821 (1985). <https://doi.org/10.1063/1.95895>
- [10] Inoue, K. High-speed all-optical gate switching experiment in a Fabry-Perot semiconductor laser amplifier. *Electron. Lett.* **23**, 921–922 (1987). <https://doi.org/10.1049/el:19870649>
- [11] González-Marcos, A. P. & Martín-Pereda, J. A. Method to analyze the influence of hysteresis in optical arithmetic units. *Opt. Eng.* **40**, 2371–2385 (2001). <https://doi.org/10.1117/1.1413747>
- [12] González-Marcos, A. P. & Martín-Pereda, J. A. Analysis of irregular behaviour on an optical computing logic cell. *Opt. Laser Technol.* **32**, 457–466 (2000). [https://doi.org/10.1016/s0030-3992\(00\)00099-2](https://doi.org/10.1016/s0030-3992(00)00099-2)
- [13] González-Marcos, A. P. & Martín-Pereda, J. A. Coder/decoder with an optical programmable logic cell. *Proc. Photonic Devices and Algorithms for Computing IV (SPIE)* **4788**, 126–134 (2002). <https://doi.org/10.1117/12.451553>
- [14] Martín-Pereda, J. A. & González-Marcos, A. P. Logic cells as basic structures to add/drop WDM information signals. *Proc. Photonic Devices and Algorithms for Computing IV (SPIE)* **4788**, 73–82 (2002). <https://doi.org/10.1117/12.451587>
- [15] Martín-Pereda, J. A. & González-Marcos, A. P. An approach to visual cortex operation: optical neuron model. in *IEEE Conference on Lasers and Electro-Opt. Europe* 355–356 (1994). <https://doi.org/10.1109/CLEOE.1994.636629>
- [16] Peng, H. T. et al. Neuromorphic photonic integrated circuits. *IEEE J. Sel. Top. Quantum Electron.* **24**, 8364605 (2018). <https://doi.org/10.1109/JSTQE.2018.2840448>
- [17] Kim, M., Kim, S. & Kim, S. Resonator-free optical bistability based on epsilon-near-zero mode. *Sci. Rep.* **9**, (2019). <https://doi.org/10.1038/s41598-019-43067-z>
- [18] Kawaguchi, H., Magari, K., Yasaka, H., M. Fukuda & Oe, K. Tunable optical-wavelength conversion using an optically triggerable multielectrode distributed feedback laser diode. *IEEE J. Quantum Electron.* **24**, 2153–2159 (1988). <https://doi.org/10.1109/3.8558>
- [19] Kawaguchi, H. Bistable operation of semiconductor lasers by optical injection. *Electron. Lett.* **17**, 741–742 (1981). <https://doi.org/10.1049/el:19810521>
- [20] Kawaguchi, H. Absorptive and dispersive bistability in semiconductor injection lasers. *Opt. and Quantum Electron.* **19**, S1–S36 (1987). <https://doi.org/10.1007/bf02034349>
- [21] Otsuka, K. & Iwamura, H. Analysis of a multistable semiconductor light amplifier. *IEEE J. Quantum Electron.* **19**, 1184–1186 (1983). <https://doi.org/10.1109/jqe.1983.1072006>
- [22] Nakai, T., Ogasawara, N. & Ito, R. Optical bistability in a semiconductor laser amplifier. *Jpn. J. Appl. Phys.* **22**, L310–L312 (1983). <https://doi.org/10.1143/jjap.22.l310>
- [23] Adams, M. J., Westlake, H. J., O'Mahony, M. J. & Henning, I. D. A comparison of active and passive optical bistability in semiconductors. *IEEE J. Quantum Electron.* **21**, 1498–1504 (1985). <https://doi.org/10.1109/jqe.1985.1072818>
- [24] Westlake, H. J., Adams, M. J. & O'Mahony, M. J. Measurement of optical bistability in an InGaAsP laser amplifier at 1.5 μ m. *Electron. Lett.* **21**, 992–993 (1985). <https://doi.org/10.1049/el:19850701>
- [25] Hurtado-Villavieja, A. Bistable photonic structures for computing and switching. (ETSIT, UPM, Polytechnic University of Madrid, 2006).
- [26] Vivero-Palmer, T.R. Analysis of Photonic Structures for Optical Networks. (ETSIT, UPM, Polytechnic University of Madrid, 2010).
- [27] Carroll, J., Whiteaway, J. & Plumb, D. *Distributed Feedback Semiconductor Lasers*. (The Institution of Electrical Engineers and SPIE - The International Society for Optical Engineering, 1998). <https://doi.org/10.1049/pbcs010e>
- [28] Ghafouri-Shiraz, H. *Distributed Feedback Laser and Optical Tunable Filters*. (John Wiley & Sons Ltd., 2003).
- [29] Morrison, G.B. et al. High Power single mode photonic integration. in *IEEE High Power Diode Lasers and Systems Conference HPD* 47, 48 (2019). <https://doi.org/10.1109/HPD48113.2019.8938603>
- [30] Liu, Y. et al. High-power AlGaInAs/InP DFB lasers with low divergence angle. in *Conference on Lasers and Electro-Optics*

Europe and European Quantum Electronics Conference CLEO/Europe-EQEC (Germany, 2019).

<https://doi.org/10.1109/cleoe-eqec.2019.8872502>

[31] Liu, S. et al. High-power single-longitudinal-mode dfb semiconductor laser based on sampled Moiré grating. *IEEE Photonics Technol. Lett.* **31**, 751–754 (2019). <https://doi.org/10.1109/LPT.2019.2906562>

[32] Guo, K. et al. Symmetric step-apodized distributed feedback fiber laser with improved efficiency. *IEEE Photonics J.* **11**, (2019). <https://doi.org/10.1109/JPHOT.2019.2921628>

[33] Wang, B., Zhou, Y., Guo, Z. & Wu, X. Design for distributed feedback laser biosensors based on the active grating model. *Sensors* **19**, 2569 (2019). <https://doi.org/10.3390/s19112569>

[34] Dhoore, S., Königer, A., Meyer, R., Roelkens, G. & Morthier, G. Electronically Tunable distributed feedback (DFB) laser on silicon. *Laser Photonics Rev.* **13**, 1800287 (2019). <https://doi.org/10.1002/lpor.201800287>

[35] Wanga, J. et al. Near-infrared methane sensor based on a distributed feedback laser. *Spectrosc. Lett.* **52**, 1–8 (2019). <https://doi.org/10.1080/00387010.2019.1569063>

[36] Guoa, Y. et al. A portable laser-based sensor for detecting h2s in domestic natural gas. *Infrared Phys. Technol.* **105**, 103153 (2020). <https://doi.org/10.1016/j.infrared.2019.103153>

[37] Hatori, N. et al. First demonstration of a hybrid integrated light source on a si platform using a quantum dot laser under wide temperature range. in *IEEE Photonics Conference* (Bellevue, USA, 2013). <https://doi.org/10.1109/IPCCon.2013.6656422>

[38] Kozlov, V. G., Bulovic, V. & Forrest, S. R. Temperature independent performance of organic semiconductor lasers. *App. Phys. Lett.* **71**, 2575–2577 (1997). <https://doi.org/10.1063/1.120186>

[39] Asryan, L. V. & Luryi, S. Semiconductor laser with reduced temperature sensitivity. US Patent no. 6,870,178 B2 (2005).

[40] Miller, D. A. B. et al. The quantum well self-electrooptic effect device: Optoelectronic bistability and oscillation, and self-linearized modulation. *IEEE J. Quantum Electron.* **21**, 1462–1476 (1985). <https://doi.org/10.1109/jqe.1985.1072821>

[41] Vivero-Palmer, T. R., Rivas-Moscoco, J. M., González-Marcos, A. P. & Martín-Pereda, J. A. Dispersive optical bistability in Quantum Wells with logarithmic gain. *IEEE J. Quantum Electron.* **46**, 1184–1190 (2010). <https://doi.org/10.1109/jqe.2010.2044974>

[42] Vivero-Palmer, T. R., Rivas-Moscoco, J. M., González-Marcos, A. P. & Pereda, J. A. M. Dispersive optical bistability in bulk InGaAsP Fabry-Pérot lasers. *Reunión Esp. de Optoelectrón. (OPTOEL) OPTOEL '09, Libro de Actas*, 209–214 (2009) [in Spanish].

[43] *VPIcomponentMaker™ Photonic Circuits User's Manual (Module Reference)*. (VPIphotonics™: 2019).

[44] González-Marcos, A. P., Campoy-Fernández, J., Alaíz-Gudín, A. M., Pacheco-Ordóñez, F. & Pedro-Carracedo, J. de Fotónica y Defensa en el Año de la Luz. *Congreso Nacional de I+D en Def. y Segur. (DESEI+D) DESEI+D 2015*, 705–714 (2015) [in Spanish].

Appendix

Table 6.
BD1 and BD2 parameters.

Name	BD1 value	BD2 value	Unit
Cavity length	400	400	µm
Active region width	2.5	2.5	µm
Active region thickness – MQW	40	40	nm
Active region thickness – SCH	210	210	nm
Current injection efficiency	1	1	-
Effective index	3.7	3.7	-
Internal loss	3000	3000	1/m
Confinement factor – MQW	0.07	0.07	-

Name	BD1 value	BD2 value	Unit
Confinement factor – SCH	0.56	0.56	-
Optical coupling efficiency	1	1	-
Grating period	210.075	210.24	nm
Grating phase shift	90	90	deg
Index grating coupling coefficient	6000	6000	1/m
Carrier density	$2.0 \cdot 10^{24}$	$2.0 \cdot 10^{24}$	$1/m^3$
Linear gain coefficient	$30 \cdot 10^{21}$	$30 \cdot 10^{21}$	m^2
Gain bandwidth	10^{12}	10^{12}	Hz
Nonlinear gain coefficient	$1.0 \cdot 10^{23}$	$1.0 \cdot 10^{23}$	m^3
Nonlinear gain time constant	$500 \cdot 10^{-15}$	$500 \cdot 10^{-15}$	s
Carrier density transparency	$1.5 \cdot 10^{24}$	$1.5 \cdot 10^{24}$	$1/m^3$
Bimolecular recombination	10^{-16}	10^{-16}	m^3/s
Auger recombination	$1.3 \cdot 10^{-41}$	$1.3 \cdot 10^{-41}$	m^6/s
Carrier capture time constant	$70 \cdot 10^{-12}$	$70 \cdot 10^{-12}$	s
Carrier escape time constant	$140 \cdot 10^{-12}$	$140 \cdot 10^{-12}$	s
Initial carrier density	$0.5 \cdot 10^{24}$	$0.5 \cdot 10^{24}$	$1/m^3$
Chirp linewidth factor	3	3	-
Spontaneous emission inversion parameter	2	2	-
Bias current	$0.3257 \cdot I_{th}$	$0.4531 \cdot I_{th}$	-
Frequency detuning	20	14.5	GHz

Meaning of each parameter:

- cavity length: length of the BD section,
- active region width: width of the active region,
- active region thickness – MQW: total thickness of the quantum wells for the MQW sections,
- active region thickness – SCH: half thickness (one-side thickness) of the separate confinement heterostructure for the MQW sections,
- current injection efficiency: in our case, there is full efficiency,
- effective index: effective index of the waveguide mode,
- internal loss: the modal power loss coefficient. This parameter takes into account the carrier-density-independent part of the modal loss,
- confinement factor – MQW: total optical confinement factor of all quantum wells for the MQW sections,
- confinement factor – SCH: optical confinement factor of the separate confinement heterostructure for the MQW sections,
- optical coupling efficiency: optical coupling efficiencies to adjacent components on the left and right facets of the device section,

- grating period: specifies the grating period. This parameter can be used for tuning the laser centre frequency,
- grating phase shift: sets the grating phase shift nominally applied at the middle of the grating,
- index grating coupling coefficient: defines the index grating coupling coefficient per unit length at the reference carrier density. The index grating is caused by periodic refractive index variations along the laser waveguide,
- carrier density: defines the reference value of the carrier density for the calculation of the index and gain (loss) grating coupling coefficients,
- linear gain coefficient: defines the gain coefficient for the active device sections using the linear gain model,
- gain bandwidth: defines the width of the frequency range within which the optical gain per unit length is positive (no absorption).
- nonlinear gain coefficient: defines the nonlinear reduction of the gain at high photon densities in the form $1/(1+\varepsilon \cdot S)$, where ε is the nonlinear gain coefficient and S is the photon density,
- nonlinear gain time constant: defines the time constant for the delayed response of the gain nonlinearity to changes in photon density,
- carrier density transparency: the carrier density value at which the material gain per unit length (or its peak value in case of the frequency-dependent gain) is zero,
- bimolecular recombination: bi-molecular (quadratic) carrier recombination coefficient ($B \cdot N^2$),
- Auger recombination: Auger (cubic) carrier recombination coefficient ($C \cdot N^3$),
- carrier capture time constant: time constant of capture and diffusion of the carriers to the quantum wells for the MQW sections,
- carrier escape time constant: time constant of escape and diffusion of the carriers from the quantum wells for the MQW sections,
- initial carrier density: initial value of the carrier density in the active region,
- chirp linewidth factor: defines the linewidth enhancement factor of the quantum wells for the active MQW sections,
- spontaneous emission inversion parameter: defines the population inversion parameter that describes the increase in spontaneous emission over that in a fully inverted system,
- bias current: polarization current of the BD,
- frequency detuning: difference between resonance frequency and frequency of the input signal.